PROCEEDINGS, 51st Workshop on Geothermal Reservoir Engineering
Stanford University, Stanford, California, February 9-11, 2026
SGP-TR-230

A Dynamic Continuum Phase-Field Framework for Electro-Hydraulic Pulse-Power Fracturing

Chunhui Zhao[1], Ahmed Elbanna[2], Rafael Villamor-Lora[3], Wencheng Jin[4]

[1]University of Illinois at Urbana-Champaign; [2]University of Southern California; [3]Eden GeoPower Inc; [4]Texas A&M University

E-mail: chunhui3@illinois.edu

Keywords: Pulsed power fracturing, Dynamic fracture propagation, Phase field modeling, Subsurface stimulation

ABSTRACT

The global transition to sustainable energy demands innovative technologies that enhance the efficiency and scalability of renewable resource utilization. Subsurface stimulation offers a promising pathway to accelerate heat exchange in geothermal reservoirs. However, conventional hydraulic fracturing technology remains constrained by packer leakage, flow short-circuiting, and limited fracture surface area. To address these challenges, dynamic fracturing using pulsed power has been proposed to enable more efficient, controllable, and sustainable stimulation of subsurface resource extraction. Pulsed power fracturing experiments have been reported in the literature, but the conversion efficiency of electrical energy into mechanical energy that drives rock fracture, especially in multiple pulses scenarios, remains insufficiently understood due to the dynamic nature of the process in microseconds. Moreover, because rocks are naturally fluid-infiltrated, the coupled interaction between fracture propagation and fluid flow has yet to be systematically analyzed and compared with pure solid description.

To address these challenges, this study introduces a three-dimensional dynamic continuum modeling framework that fully couples the phase-field fracture method with fluid flow and evolving hydro-mechanical properties. Using empirical relationships extracted from existing literature, we capture the fracturing dynamics on the microsecond timescale, representing the pulse power as a time-dependent, depth-varying mechanical pressure applied on the borehole boundary. The implementation is validated against laboratory experiments on both dry and fluid-saturated rock samples. Finally, we evaluate the governing factors controlling fracture surface enhancement and energy conversion efficiency. We assess the complete energy budget under multiple pulsing conditions. The findings provide insights into the fundamentals of pulsed power fracturing, reveal energy partitioning mechanisms, and identify key factors to improve efficiency and scalability to field applications.

1. INTRODUCTION

The global transition to sustainable energy is creating an urgent demand for innovative technologies that improve the efficiency and scalability of geothermal resources. Subsurface stimulation is central to this effort, as it can increase fracture surface area by several orders of magnitude, thereby enhancing heat exchange in geothermal reservoirs.

However, conventional hydraulic fracturing technologies remain constrained by packer leakage (Abid et al., 2022; Quinn, 2009) and flow short-circuiting (Cao et al, 2025; Liu et al, 2024a). To address these challenges, electro-hydraulic fracturing like pulsed-power fracturing, enabling more efficient, controllable, and sustainable subsurface resource stimulation (Zhang et al, 2024; Soliman et al, 2024). There are mainly two types of pulsed power processes (Rao et al. 2023): (1) electrical fragmentation, where plasma channel is generated directly within the rock and (2) liquid-electrical fragmentation that fractures the rock sample through shock wave generated by plasma-liquid interaction. In this study, we focus on the second approach with simplified pulse loading to investigate the fracture generation processes within the rock sample.

The fundamental mechanisms of plasma channel formation and the conversion of electrical energy into mechanical, chemical, and thermal energy in pulsed power fracking are not yet fully understood, particularly regarding multi-physical field coupling process (Xiao, 2017), energy generation mechanisms of shock waves (Zhang et al, 2025), and mechanical behavior under realistic reservoir conditions with confining stresses (Agarwal et al, 2023; Soliman et al, 2024). Although there are attempts on theoretical derivation for energy conversion (Wu et al, 2022a), pulsed power has typically been simplified by replacing the plasma channel with a mechanical pulse, act as a pressure boundary condition to drive the fractures. The empirical law of peak value, pulse shape are determined by experiments (Touya et al., 2006; Cao and Younis, 2024). Despite this simplification, only a few studies have explored pulsed power fracture modeling in the literature. For instance, Meng et al, (2023) employed the splitting method to simulate pulsed power fractures, but this approach is limited by the need to preset the fracture path. To overcome this limitation, the combined finite-discrete element method (FDEM), which incorporates cohesive/interface elements throughout the mesh, has been used in tools like Irazu and HOSS to model pulse-induced dynamic fracturing (Cao and Younis, 2024; Soliman et al 2024). However, major questions remain: (1) coupling of fracture propagation with fluid flow for saturated rock sample and (2) effectiveness of multi-pulses on fracture surfaces enhancement.

On the other hand, phase field approach has successfully incorporated fully coupled hydro-mechanical formulation, together with consistent damaged-induced hydraulic properties evolution (Li et al., 2024; Yu et al., 2024; Kou et al, 2025). Phase-field fracture offers several advantages: its energy-minimization framework does not require a prescribed crack path (Kristensen et al., 2021), and its inherent non-locality mitigates mesh dependence (Mandal et al., 2019), and it has shown capability to adopt advanced non-linear constitutive models (Miehe et al., 2017) and easy extension to existing THM (thermo-hydro-mechanical) multi-physical coupling (Liu et al., 2024; Dai et al., 2024). These features make it an attractive approach for modeling pulsed-power fracturing processes.

This paper presents a computational framework for simulating pulsed power fracturing an MOOSE App. MOOSE stands for Multiphysics Object-Oriented Simulation Environment framework, which is an open-source, finite-element, parallel computing platform developed at Idaho National Laboratory (Giudicelli et al., 2024). We extend the phase field framework from RACCOON (Hu et al., 2020) by deriving and implementing a fully coupled hydro-mechanical formulation with damage-dependent hydraulic properties.

The paper is organized as follows. Section 2 presents the theoretical foundation, including the variational formulation, governing equations and boundary conditions, evolution laws for hydraulic properties (permeability, porosity, and Biot coefficient), and the characterization of pulse loading parameters. Section 3 describes the energy budget calculations, Section 4 validates the model against laboratory experiments by simulating three-dimensional specimens under both dry and fully saturated conditions. Finally, Section 5 highlights the key contributions of this work, explains the current model limitations and provides directions for future work.

2. MODELING APPROCH

In this section, we begin with the variational formulation and governing equations of the phase-field method and document the damage dependent poroelastic properties.

2.1 Variational formulation of phase field method

The potential energy Ψ is the summation of elastic strain energy Ψ^e, kinetic energy Ψ^k, dissipation energy Ψ^d as fracture propagates, energy stored in fluid Ψ^f and the external energy input Ψ^s:

$$\Psi = \Psi^e + \Psi^k + \Psi^d + \Psi^f - \Psi^s \tag{1}$$

2.1.1 Elastic strain energy Ψ_e

As described in Miehe et al., (2010a), The elastic strain energy Ψ^e adopts an anisotropic formulation due to fact that pulsed power fracturing is predominantly Mode I open crack, with the assumption that only tensile strength can be reached, to avoid unrealistic damage in compressive regime:

$$\Psi^e = \int_\Omega \psi^e(\epsilon(u), d)dV = \int_\Omega [\omega(d)\psi_o^{e+}(\epsilon) + \psi_o^{e-}(\epsilon)] \tag{2}$$

Where the degradation function $\omega(d) = (1-d)^2$. The ψ_o^{e+} is the undamaged tensile elastic energy, ψ_o^{e-} is the inactive portion of energy during fracture propagation. The definitions are as follows (i,j,m = 1,2,3, summation applies):

$$\psi_o^e(\varepsilon) = \frac{\lambda}{2}(\varepsilon_{mm})^2 \ + \ \mu\varepsilon_{ij}\varepsilon_{ij} \tag{3}$$

$$\psi_o^{e+}(\varepsilon) = \frac{\lambda}{2}\left\langle\sum_{a=1}^{\delta}\varepsilon_a\right\rangle_+^2 \ + \ \mu\sum_{a=1}^{\delta}\left\langle\varepsilon_a\right\rangle_+^2 \tag{4}$$

$$\psi_o^{e-} = \psi_o^e(\varepsilon) - \psi_o^{e+}(\varepsilon) \tag{5}$$

The spectral decomposition of strain tensor is applied on equation (4), where $\langle x\rangle_+$ represents the Macaulay operator:

$$\left\langle x\right\rangle_+ = \frac{1}{2}(x + |x|) \tag{6}$$

ε_a is the tensile part of the principal strain (a = 1, 2, 3):

$$\epsilon^+ = \mathbf{V}\,\mathbf{\Lambda}^+\,\mathbf{V}^\top \tag{7}$$

Where V is eigenvectors of strain tensor, and $\Lambda^+ = \mathrm{diag}(\{\lambda_i\}^+)$, i = 1, 2, 3 is the positive part of the diagonal eigenvalue matrix. The degradation function and stiffness degradation is only applied on the tensile portion of elastic energy. The effective Cauchy stress tensor $\boldsymbol{\sigma}'$, stress taken by solid skeleton, is defined as follows:

$$\sigma' = \frac{\partial\psi^e}{\partial\epsilon} = \omega(d)\sigma^+ + \sigma^- \tag{8}$$

Where the positive part of stress tensor $\boldsymbol{\sigma}^+$:

$$\sigma^{+} = \lambda\{\epsilon_{mm}\}_{+}\delta_{ij} + 2\mu\epsilon_{ij}^{+} \tag{9}$$

2.1.2 Dissipated energy during crack propagation Ψ^d

The dissipated energy follows Wu (2017):

$$\Psi^d = \int_\Omega G_f \gamma(d, \nabla d) dV = \int_\Omega \frac{G_f}{c_\alpha}[\frac{1}{l}\alpha(d) + l(\nabla d \cdot \nabla d)] dV \tag{10}$$

Where G_f is critical fracture energy. In this study, we adopt classical AT1 model, which possess an elastic domain before the damage initiation (Wu 2017; Gupta et al., 2022). In AT1 model, the geometric crack function $\alpha(d) = d$, and the scaling parameter $c_\alpha = 8/3$. l is the internal length scale.

2.1.3 Kinetic energy Ψ^k

The kinetic energy Ψ^k is associated with solid skeleton, with its function given as:

$$\Psi^k = \int_\Omega \frac{1}{2}\rho^s \dot{u}\dot{u} dV \tag{11}$$

Where u is the displacement of the solid skeleton, ρ^s is the solid density.

2.1.4 Fluid driving energy Ψ^f

The fluid driving energy is expressed as in Miehe and Mauthe (2016):

$$\Psi^f = \int_\Omega \frac{M}{2}\Big(\big(\beta \mathrm{tr}\,\boldsymbol{\varepsilon}\big)^2 - 2\,\beta\,\theta\,\mathrm{tr}\,\boldsymbol{\varepsilon} + \theta^2\Big) dV = \int_\Omega \frac{M}{2}\big(\theta - \beta \mathrm{tr}\,\boldsymbol{\varepsilon}\big)^2 dV \tag{12}$$

Where M is Biot modulus, β is the Biot coefficient, and θ represents the increment of fluid content. The pore fluid pressure p is defined as $p = \partial\Psi^f/\partial\theta = M(\theta - \beta\,\mathrm{tr}\,\varepsilon)$, re-arrange the equation, we have the definition for fluid content θ:

$$\theta = \frac{p}{M} + \beta \nabla \cdot u \tag{13}$$

2.1.5 External energy Ψ^s

The external energy consists of work done by body force b or boundary traction t:

$$\Psi^s = \int_\Omega b \cdot u dV + \int_\Omega t \cdot u dA \tag{14}$$

2.2 Governing equation

2.2.1 Strong form (u,p,d)

In the phase field approach, energy minimization on total energy (1) we have:

$$\begin{aligned} \nabla \cdot \boldsymbol{\sigma} + \mathbf{f} &= \rho^s \ddot{\mathbf{u}} \quad \text{in} \quad \Omega \\ \beta \dot{\epsilon}_v + \frac{1}{M}\dot{p} + \nabla \cdot \mathbf{q} &= s_q \quad \text{in} \quad \Omega \\ \frac{G_f}{c_\alpha}\left(\frac{1}{l}\alpha'(d) - 2l\Delta d\right) &= (1-d)H^{+} \quad \text{in} \quad \Omega \end{aligned} \tag{15}$$

Where the maximum history energy H^+:

$$H^{+} = \max_{t\in[0,T]}\left(\left\langle 2\psi_o^{e+} + p^2[(\phi_o - 1)(\frac{1}{K_f} - \frac{1}{K_s}) - \frac{K}{K_s^2}]\right\rangle^{+}\right) \tag{16}$$

Looking at the form of H^+, the first term is standard in classical phase field formulation (Miehe et al, 2010b), second term involves the poroelastic properties, which is the resultant of damage dependence on porosity, Biot coefficient and Biot modulus. The same form H^+ has been derived in recent papers as well (Yu et al, 2024). The prescribed boundary conditions on Dirichlet (Γ^u, Γ^p) and Neumann (Γ^t, Γ^q) surfaces are given as follows:

$$\begin{cases} u = \bar{u} & on\ \Gamma^u \\ \sigma n = \bar{t}_s & on\ \Gamma^t \\ p = \bar{p} & on\ \Gamma^p \\ q \cdot n = \bar{q} & on\ \Gamma^q \end{cases} \tag{17}$$

Where σ, f, ρ^s are total stress tensor, body force, solid skeleton density. ε_v, q and $\overline{q}$ are volumetric strain of the solid skeleton, flux of the fluid flow and flow source in the bulk matrices. The total stress **σ** is taken by both solid skeleton and pore pressure (weighted by Biot coefficient β):

$$\sigma = \sigma' + \beta p \tag{18}$$

The flux q relates gradient of pressure via Darcy's law:

$$\mathrm{q} = - \kappa \nabla p = \frac{k}{\mu_f} \nabla p \tag{19}$$

κ is the hydraulic conductivity, k is the intrinsic permeability and μ_f is the fluid viscosity.

2.2.2 Weak form

The weak form of equation (15) is given as follows, (ψ_u, ψ_p, ψ_d) is the testing functions for trial functions (**u**,p,d), respectively:

$$\begin{aligned} &\int_\Omega \sigma' \nabla \psi_u \, dv - \int_\Gamma \sigma' \cdot n \psi_u \, d\Gamma - \int_\Omega \alpha p \nabla \cdot \psi_u \, dv + \int_\Omega f \psi_u \, dv - \int_\Omega \rho^s \ddot{\mathbf{u}} \psi_u \, dv = 0 \\ &\int_\Omega \alpha \frac{\Delta \epsilon_v}{\Delta t} \psi_p dv + \int_\Omega \frac{1}{M} \frac{\Delta p}{\Delta t} \psi_p dv - \int_\Omega q \cdot \nabla \psi_p dv - \int_\Omega s_q \psi_p dv + \int_\Gamma q n \psi_p d\Gamma = 0 \\ &\int_\Omega \left[\omega'(d) \, H^+ \psi_d \; + \; \frac{G_f}{c_\alpha} \left(\frac{\alpha'(d)}{b} \, \psi_d \; + \; 2 \, b \, \nabla d \cdot \nabla \psi_d \right) \right] \mathrm{d}V \; \geq \; 0 \end{aligned} \tag{20}$$

Where volumetric strain rate d(ε_v)/dt and pressure rate d(p) /dt are approximated as its increments $\Delta\varepsilon_v$, Δp divided by time step Δt. n is the surface normal after integration by part, positive as pointing outward.

2.3 Absorbing boundary condition

In the laboratory experiments, samples are radially confined using plastic ties, which dissipate outgoing stress waves and suppress wave reflection at the specimen boundary to avoid spallation. To replicate these conditions numerically, we apply absorbing boundary conditions based on the Lysmer damper formulation (Lysmer and Kuhlemeyer, 1969) at the outer boundaries of both the three-dimensional laboratory model and the two-dimensional parametric study domain. This approach minimizes wave reflection at the model boundaries.

2.4 Hydraulic properties evolution

2.4.1 Darcy-poiseuille permeability

The model adopts Darcy-Poiseuille permeability (Miehe and Mauthe, 2016) for damage-induced enhancement. The total permeability k is a tensor quantity of the intact matrix permeability $\mathbf{k}_m$ and the damage zone $\mathbf{k}_f$, follows (Li et al., 2024; Miehe and Mauthe, 2016):

$$\mathbf{k} = \mathbf{k}_m + d^e \left(\mathbf{k}_f - \mathbf{k}_m \right) \tag{21}$$

Where d^e is the exponential function of crack damage field, e is a constant. The intact matrix permeability is assumed to be isotropic $\mathbf{k}_m = \mathbf{k}_o\mathbf{I}$. And the damage zone permeability tensor is related to aperture of crack: $\mathbf{k}_f = w(d)^2/12\ \mathbf{I}$, where $w(d) = dG_f/f_t$. f_t is the tensile strength of the material. Note in AT1 model, the energy release rate G_f and tensile strength f_t are related through length scale *l*:

$$\mathrm{f}_t = \sqrt{3 \, E \, G_f / (8l)} \tag{22}$$

In this study, we assume G_f as material property and use realistic rock material value, the f_t is determined by specific usage of characteristic length scale *l*.

2.4.2 Biot coefficient, porosity and Biot modulus

During the fracture process, hydraulic properties vary with damage. Following earlier work (Yu et al., 2024; Mobasher et al., 2017), the Biot coefficient β(d) is assumed to evolve with damaged solid bulk modulus $K_d = \omega(d)K$:

$$\beta(d) = 1 - \frac{K_d}{K_s} = 1 - \frac{\omega(d)K}{K_s} \tag{23}$$

Where K_s is the bulk modulus of solid grains, which is treated as material property. The porosity φ(d) increases with damage, adopting the following relation (Yu et al., 2024; Kou et al., 2025):

$$\phi(d) = \phi_o + (1 - \phi_o)[1 - \omega(d)] \tag{24}$$

Both damaged Biot coefficient β(d) and porosity φ(d) are used to modify the Biot modulus M(d) as follows:

$$1/\mathrm{M(d)} = \phi(d)/K_f + (\beta(d) - \phi(d))/K_s \tag{25}$$

Where K_f is the fluid bulk modulus.

3. ENERGY MEASUREMENT

We implement the above governing equations, constitutive laws, properties evolution to perform pulsed power dynamic simulation. During the pulsed power fracturing process, we track different energy components, and achieve energy conservation in the process, the definitions are shown as follows:

3.1 Fracture energy

The energy driving for crack propagation in phase field is defined in equation (10):

$$\mathrm{E}^f = \int_\Omega \frac{G_f}{c_\alpha}\left[\frac{1}{l}\alpha(d) + l(\nabla d \cdot \nabla d)\right]dV \tag{26}$$

3.2 Elastic energy

The elastic energy in the solid skeleton is defined in equation (2):

$$\mathrm{E}_s^e = \int_\Omega [\omega(d)\psi_o^{e+}(\epsilon) + \psi_o^{e-}(\epsilon)] \tag{27}$$

For the fluid elastic energy, we have:

$$\mathrm{E}_f^e = \int_\Omega \frac{1}{2}\alpha p \epsilon_{ii} dV \tag{28}$$

Where α is the Biot coefficient, p is the pore pressure, ε_{ii} is the trace of elastic strain (i = 1,2,3, summation applies).

3.3 Kinetic energy

The kinetic energy in solid skeleton is defined as:

$$\mathrm{E}_s^k = \int_\Omega \frac{1}{2}\rho_s v_s^2 dV \tag{29}$$

And in fluid, we use Darcy velocity (flux) $v_f = -(k/\mu)\nabla p$ as representation of fluid velocity and calculate its kinetic energy:

$$\mathrm{E}_f^k = \int_\Omega \frac{1}{2}\rho_f v_f^2 dV \tag{30}$$

3.4 Fluid dissipation energy

The fluid dissipation energy is computed as follows:

$$\mathrm{E}_f^d = \int_\Omega \int_t \alpha p \epsilon_{ii} dT\ dV - \int_\Omega \frac{1}{2} p \epsilon_{ii} dV \tag{31}$$

3.5 Total boundary input energy

The total input energy applied from the boundary via pulsed power or confinement pressure is estimated using the surface integral of the confinement pressure applied in the boundary surface times the normal displacements of the surface.

$$\mathrm{E}^i = \int_\Gamma P(u \cdot n) dS \quad (32)$$

Table 1: Material and loading parameters used in this study.

Parameter Name	**Value**
Young's Modulus E	50 GPa
Poisson's Ratio ν	0.3
Density ρ	2600 $\mathrm{kg/m^3}$
Critical Fracture Energy G_c	40 $\mathrm{J/m^2}$
Initial Permeability κ_0	5×10^{-19} $\mathrm{m^2}$
Initial Porosity ϕ_0	0.8%
Initial Biot Coefficient β_0	0.167
Fluid Bulk Modulus K_f	2.24 GPa
Fluid Viscosity μ	1×10^{-3} $\mathrm{Pa \cdot s}$
Fluid Density ρ_o	1000 $\mathrm{kg/m^3}$
Single Pulse Duration t_p	10 μs
Number of Pulses n	Varying, specific in each case
Sample Outer Diameter W	25 mm
Sample Inner Diameter D	3.2 mm
3D Sample Height H	60 mm
3D Sample Gap G	8 mm
Hydrostatic Confinement Pressure P_o	Varying, specific in each case
Initial Pore Pressure p_0	0.0965 MPa (0 MPa in pure solid case)
Length Scale l	Varying, specific in each case
Mesh Size Δx	Varying, specific in each case
Time Step Δt	Varying, specific in each case

4.RESULTS AND DISCUSSIONS

In this section, we conduct numerical analyses on both dry samples (solid displacement and damage) and fluid-saturated samples (solid skeleton displacement, pore pressure, and damage) under multiple pulse loading conditions. In Section 4.1, we validate the 3D model against available laboratory experimental results. Table 4.1 summarizes the parameters used in this study. Material properties of Sierra White Granite and laboratory sample dimensions are extracted directly from experimental data, while mesh size, time step, and phase field length scale are model parameters constrained by the physical sample size and desired simulation resolution. The length scale is chosen to be 2–3 times the mesh size to ensure the damage band is fully resolved.

4.1 Model validation

4.1.1 Problem Setup

We consider both dry samples (pure solid) and fluid-saturated samples (hydro-mechanical coupling) under undrained conditions. The laboratory sample geometry is illustrated in Figure 1(a)–(b). Figure 1(a) shows a three-dimensional cylindrical sample of diameter W, initially in equilibrium under pore pressure p_0 (p_0 = 0.0965 MPa for the fluid-saturated case, in agreement with lab reported value). The sample contains a central borehole of diameter D, within which two electrodes are positioned (shown as grey bars). In the experiment, this borehole is filled with water to provide necessary environment for plasma generation; however, the fluid within the borehole is not explicitly modeled. Wave-absorbing boundary conditions are applied to the outer, top, and bottom surfaces to minimize wave reflections and prevent spallation. The outer boundary is subjected to a confining pressure P_o (P_o = 0 MPa for the unconfined pure solid case; P_o = 1 MPa for the confined fluid-saturated case). Since the standard phase field model is insufficient for predicting crack nucleation (Kumar et al., 2020), we introduce four weak nucleation planes near the borehole, each extending 0.4 mm radially outward from the borehole surface with an initial damage value of d = 0.9, as indicated in green region.

Figure 1(b) provides a zoom-in view of the gap region G between the two electrodes. During the experiment, plasma is generated through fluid-electrical-chemical interactions within this gap, produces shock waves that travels through the borehole fluid and into the surrounding rock, inducing fracture (Rao et al., 2023). Rather than explicitly modeling this complex multi-physics process, which remains incompletely understood, we adopt experimentally calibrated pulse shape and peak pressure functions (Touya et al., 2006; Cao and Younis, 2024) applied as pressure boundary conditions on the borehole surface. Under multi-pulses condition, each pulse duration is assumed as t_D=10μs, and the subsequent pulse is applied right after t=t_D without any gap in time. As illustrated in Figure 2(b), the peak pressure Pp of each pulse decays as a function of radial distance r, which is the direct distance from sample center where the

plasma is generated, to the boundary of the inner borehole. We employ a phase field characteristic length scale l = 0.5 mm with mesh size h = 0.2 mm with time step Δt = 0.01 μs. To march the dynamic system with full inertia in time, we adopt implicit Newmark-Beta time integration scheme, where displacement and velocity are updated as $\mathbf{u}_{n+1} = \mathbf{u}_n + \Delta t\, \dot{\mathbf{u}}_n + (\Delta t^2/2)[(1-2\beta)\ddot{\mathbf{u}}_n + 2\beta\ddot{\mathbf{u}}_{n+1}]$; $\dot{\mathbf{u}}_{n+1} = \dot{\mathbf{u}}_n + \Delta t[(1-\gamma)\ddot{\mathbf{u}}_n + \gamma\ddot{\mathbf{u}}_{n+1}]$. The standard trapezoidal rule (β=0.25, γ=0.5) provides second-order accuracy and unconditional stability.

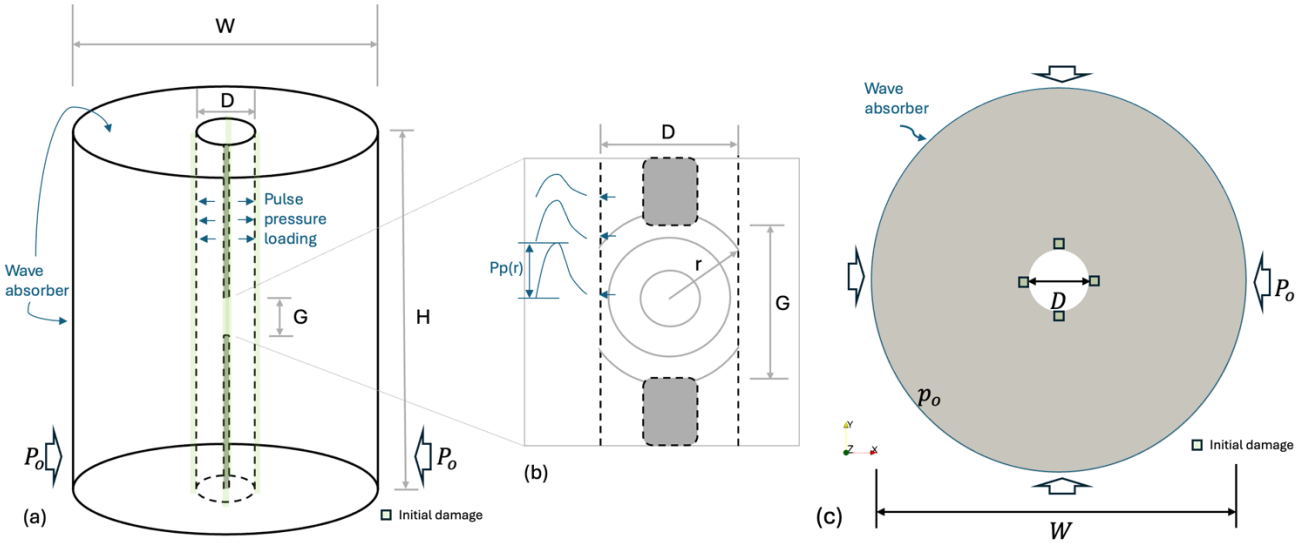

Figure 1: Modeling geometry of pulse power sample.

4.1.2 Dry sample

Figure 2 presents the temporal evolution of fracture planes during pulsed power loading for the dry sample. Figures 2(a)–(d) display the numerically predicted crack surfaces, visualized as regions where the damage variable reaches its maximum value (d = 1), shown in both full three-dimensional view and at selected vertical cross-sections. Figures 2(e)–(f) show the corresponding experimental observations obtained through visual inspection and CT scanning. The simulation successfully captures the key fracture characteristics: cracks nucleate from the borehole center, propagate radially through the sample, and extend along the axial direction. The three-dimensional fracture morphology predicted by the numerical model shows quantitative agreement with the CT scan reconstructions in Figure 2(g). Figure 2(a)-(d) figures in the second column demonstrate that the model predicts multiple straight radial cracks emanating from the borehole, consistent with CT scans at corresponding depths in Figure 2(g). The results also capture curved fracture planes, which is possibly due to interactions of stress field from nearby fractures. Figure 3 presents the energy budget computed from the numerical simulation for the first two loading pulses, with 5J applied for each pulse. The total energy comprises kinetic energy, elastic strain energy, and dissipated energy associated with crack propagation. The numerical framework satisfies energy conservation, as demonstrated by the agreement between the total input energy and full energy, which is the summation of energy components (upper subplot). The lower subplot reveals the characteristic energy partitioning captured by the simulation: pulse-like oscillations in kinetic and elastic energies during each loading cycle, accompanied by stepwise, monotonic accumulation of fracture dissipation energy as crack propagates.

The results of dry sample shown in Figure 2 and Figure 3 provide a fundamental validation of proposed model capability to capture the evolution within microseconds, which otherwise will not be recorded in experiments. Under multi-pulse loading conditions, the numerical framework seamlessly extends fracture planes from pre-existing damage generated by previous pulses, without requiring intermediate steady-state solves, remeshing, or manual intervention between successive loading cycles. This continuous simulation capability is essential for modeling realistic pulsed power fracturing operations, where multiple pulses are applied in rapid succession and the cumulative fracture network evolves progressively. The demonstrated energy conservation across multiple pulses confirms the numerical stability and accuracy of the time integration scheme under repeated dynamic loading, establishing confidence in the model's predictive capability for extended multi-pulse simulations relevant to field-scale applications.

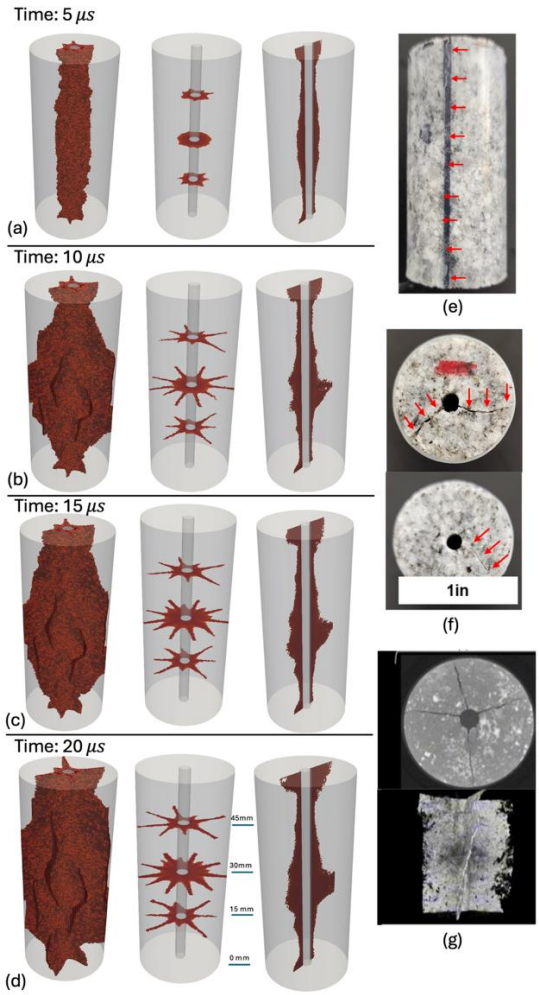

Figure 2: Fracture pattern for three-dimensional laboratory numerical simulations and experimental results for dry sample.

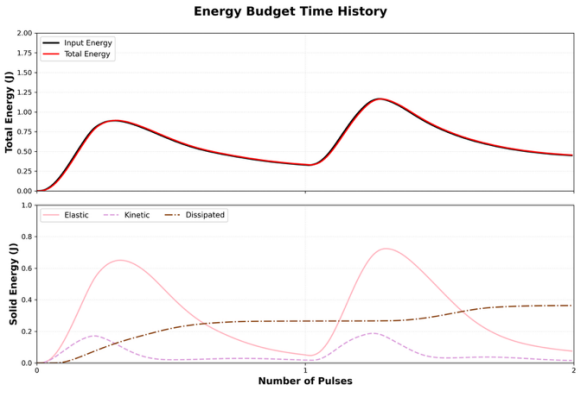

Figure 3: Energy budget for three-dimensional pure solid lab experiment

4.1.3 Fluid saturated sample

Figure 4 illustrates the evolution of damage and hydraulic properties in a fluid-saturated rock sample under pulsed power loading, with an input mechanical energy of E_B = 25 J (for each pulse) and undrained conditions imposed at the borehole boundary. Figures 4(a) display the fracture planes and depth slices, revealing a key distinction from the dry case: the crack band extends most significantly after the first pulse, with diminishing increments in subsequent pulses. This behavior arises because the presence of pore fluid absorbing a portion of the incoming wave energy, reducing the energy available to drive continued fracture propagation. Additionally, the crack bands exhibit greater width compared to the pure solid case, a direct consequence of the hydraulic property evolution. Figures 4(b) presents time snapshots of pore pressure evolution after each pulse, demonstrating the model's capability to resolve pore pressure

dynamics at the microsecond scale. The model reveals negative pore pressure due to dilatancy-induced suction under tensile loading, which promotes further crack extension before gradually relaxing. Finally, the energy budget analysis in Figure 4(c) confirms that energy conservation is satisfied between the input energy and the total energy, which encompasses contributions from both the solid and fluid phases. The dissipated energy governing fracture growth increases monotonically in a stair-step fashion with each pulse, while the elastic and kinetic energies exhibit pulse-like temporal signatures that mirror the input loading. Notably, most of the input energy is stored as elastic strain energy in the solid.

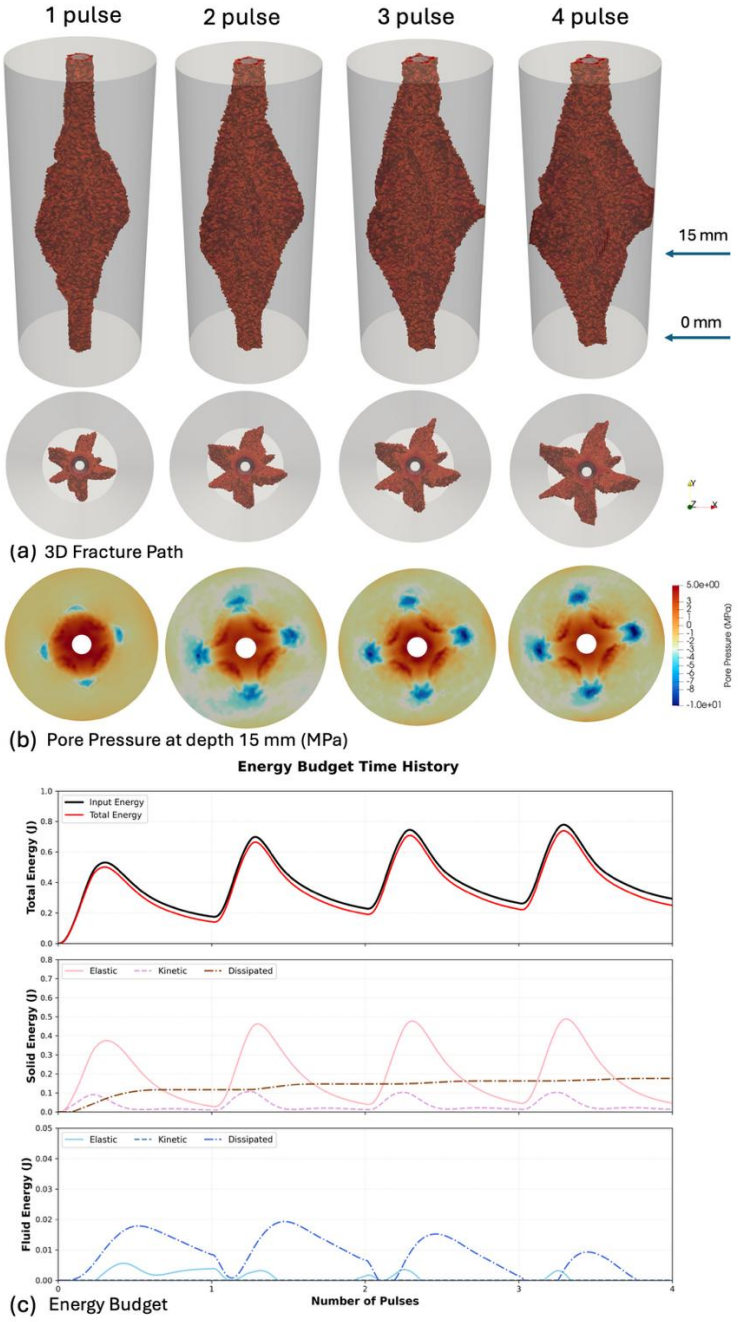

Figure 4: Three-dimensional laboratory numerical simulations for saturated rock sample.

5. CONCLUSION AND FUTURE WORK

In this study, we developed a fully coupled hydro-mechanical phase-field formulation in which hydraulic properties (porosity, Biot coefficient, and Biot modulus) evolve consistently with damage. We imposed empirically based pulse loading on the borehole boundary and conducted dynamic fracturing simulations with full inertia. The model was validated against three-dimensional lab-scale experiments for both dry and fluid saturated sample with detailed energy budget calculation.

Our 3D lab-scale simulations can capture the fracture evolution in both dry and fluid saturated samples: simulation results in pure solid case show that fractures firstly nucleate and concentrate near the center of the specimen, where the plasma releases its energy, and rapidly extend through the sample to form planar fracture planes, extend first to the outer boundary of the specimen, and propagates upwards after, this microsecond evolution cannot be otherwise obtained from experiments. The energy budget analysis achieves desired energy balance and shows step-like dissipation energy growth and pulse-like shape of kinetic and elastic energy. In the hydro-mechanical simulations, the presence of fluid phase dissipates significant of incoming wave energy, and damage-induced evolution of hydraulic properties results in stiffness loss in solid skeleton and fluid transport within fracture paths, which diminishes the efficiency of fracture propagation compared with pure solid case. On the microsecond scale of the applied pulses, the model can capture negative pore pressures evolution at crack tips due to the tensile fractures. The elastic, fluid, and total mechanical energy in energy budget graph exhibit similar pulse-like temporal signatures characteristic of fully inertial dynamics, while the dissipated (fracture) energy grows irreversibly in a stair-like fashion.

This work primarily aims to characterize fracture propagation and energy partitioning in rock specimens subjected to pulse-power loading. To make the problem tractable, we simplify the plasma–fluid interaction and explosion process, which is inherently a coupled physical-chemical phenomenon requiring additional multi-physics modeling and tighter experimental constraints. As a result, fully predictive simulations of the entire energy-conversion chain remain an open challenge. We also note the material heterogeneity plays an important role in fracture propagation. In the current study, we focus on understanding the essential idea of dynamic process, and the code is easy to adopt heterogeneity for future analysis. The scalability to field scale simulation is also an interesting future work, which could provide guidance on the field operations.

Overall, this study provides a consistent framework for modeling pulsed power fracturing, tracking both 2D and 3D fracture evolution, as well as energy partitioning, offering physical insight into how to enhance fracture surface area and design more effective field-scale stimulation strategies.

7. ACKNOWLEDGEMENT

The information, data, or work presented herein was funded in part by the Advanced Research Projects Agency-Energy (ARPA-E), U.S. Department of Energy (DOE), under Award Number DE-AR0001584. Any opinions, findings and conclusions, or recommendations expressed in this material are those of the authors and do not necessarily reflect those of the DOE or the U.S. Government.

8. REFERENCES

K. Abid, A. Sharma, S. Ahmed, S. Srivastava, A. Toledo Velazco, C. Teodoriu, A review on geothermal energy and hpht packers for geothermal applications, Energies 15 (19) (2022) 7357.

P. Quinn, High resolution packer testing in fractured sedimentary rock, Ph.D. thesis, University of Waterloo (2009).

Y. Cao, B. Feng, Z. Cui, X. Duan, J. Zhao, Numerical simulation study of segmented hydraulic fracturing in horizontal wells of fractured hot dry rocks, at the us forge site, Geoenergy Science and Engineering 249 (2025) 213790.

Y. Liu, H. Wu, A. D. Taleghani, K. Zhang, J. Zhang, M. Yang, B. Zhang, Effects of temperature-dependent viscosity on thermal drawdown-induced fracture flow channeling in enhanced geothermal systems, Renewable Energy 235 (2024) 121274.

S. Liu, K. Ji, M. Jin, Review of techniques to mitigate thermal breakthrough in enhanced geothermal systems (2025).

P. Rao, W. Feng, P. Ouyang, J. Cui, S. Nimbalkar, Q. Chen, Formation of plasma channel under high-voltage electric pulse and simulation of rock-breaking process, Physica Scripta 99 (1) (2023) 015604.

Y. Xiao, Pulsed power plasma stimulation-experimental and numerical study on single-pulse test, Ph.D. thesis (2017).

Z. Wu, P. Rao, S. Nimbalkar, Q. Chen, J. Cui, P. Ouyang, A semi-analytical solution for shock wave pressure and radius of soil plastic zone induced by lightning strikes, Materials 15 (6) (2022) 2239.

G. Touya, T. Reess, L. Pecastaing, A. Gibert, P. Domens, Development of subsonic electrical discharges in water and measurements of the associated pressure waves, Journal of Physics D: Applied Physics 39 (24) (2006) 5236.

W. Cao, R. M. Younis, Empirical scaling of formation fracturing by high-energy impulsive mechanical loads, International Journal of Rock Mechanics and Mining Sciences 173 (2024) 105613.

C. Meng, A. Fournier, W. Jin, A split-node method for modeling pulse and hydraulic fracturing, in: ARMA US Rock Mechanics/Geomechanics Symposium, ARMA, 2023.

M. Y. Soliman, A. Rezaei, M. Khalaf, P. Gordon, C. Cipolla, Pulse power plasma stimulation: A technique for waterless fracturing, Gas Science and Engineering 122 (2024) 205201.

H. Li, Z. Yang, F. An, J. Wu, Simulation of dynamic pulsing fracking in poroelastic media by a hydro-damage-mechanical coupled cohesive phase field model, Engineering Geology 334 (2024) 107502.

S. Yu, Y. Song, S. Wang, Y. Xiao, J. Hu, Y. Wang, L. Yi, Z. Yang, Novel phase field model of hydraulic fracture propagation in poroelastic media, Petroleum 10 (4) (2024) 672–695.

M. Kou, C. Li, Y. Wang, F. Liu, Phase field modelling of the hydro-mechanical coupling failure mechanisms of fissured rock masses, Frontiers in Earth Science 13 (2025) 1655762.

G. Giudicelli, A. Lindsay, L. Harbour, et al., 3.0-moose: Enabling massively parallel multiphysics simulations, SoftwareX 26 (2024) 101690.

T. Hu, J. Guilleminot, J. E. Dolbow, A phase-field model of fracture with frictionless contact and random fracture properties, Computer Methods in Applied Mechanics and Engineering 368 (2020) 113106.

C. Miehe, F. Welschinger, M. Hofacker, Thermodynamically consistent phase-field models of fracture, International journal for numerical methods in engineering 83 (10) (2010) 1273–1311.

J.-Y. Wu, A unified phase-field theory for the mechanics of damage and quasi-brittle failure, Journal of the Mechanics and Physics of Solids 103 (2017) 72–99.

A. Gupta, U. M. Krishnan, T. K. Mandal, R. Chowdhury, V. P. Nguyen, An adaptive mesh refinement algorithm for phase-field fracture models, Computer Methods in Applied Mechanics and Engineering 399 (2022) 115347.

C. Miehe, S. Mauthe, Phase field modeling of fracture in multi-physics problems. part iii, Computer Methods in Applied Mechanics and Engineering 304 (2016) 619–655.

C. Miehe, M. Hofacker, F. Welschinger, A phase field model for rate-independent crack propagation, Computer Methods in Applied Mechanics and Engineering 199 (45-48) (2010) 2765–2778.

J. Lysmer, R. L. Kuhlemeyer, Finite dynamic model for infinite media, Journal of the Engineering Mechanics Division 95 (4) (1969) 859–878.

E. Mobasher, L. Berger-Vergiat, H. Waisman, Non-local formulation for transport and damage in porous media, Computer Methods in Applied Mechanics and Engineering 324 (2017) 654–688.

D. Santillán, R. Juanes, L. Cueto-Felgueroso, Phase field model of hydraulic fracturing in poroelastic media, Journal of Geophysical Research: Solid Earth 123 (3) (2018) 2127–2155.

M. Hofacker, C. Miehe, Continuum phase field modeling of dynamic fracture, International journal of fracture 178 (1) (2012) 113–129.

Zhang Y, Wang J, Xue Q, Liu J, Li H, Fang S. Research Status and Prospects of High-Voltage Pulse Plasma Rock-Fracturing Technology. *Applied Sciences*. 2024; 14(16):7261. https://doi.org/10.3390/app14167261

Soliman, M. Y., Rezaei, A., Khalaf, M., Gordon, P., & Cipolla, C. (2024). Pulse power plasma stimulation: A technique for waterless fracturing, enhancing the near wellbore permeability, and increasing the EUR of unconventional reservoirs. Gas Science and Engineering, 122, 205201.

Zhang, Z., Nie, B., Ma, C., Liu, X., Li, Y., & Li, C. (2025). A study of high-intensity high voltage electric pulse fracturing-A perspective on the energy distribution of shock waves. Geoenergy Science and Engineering, 249, 213791.

Agarwal, M., & Kudapa, V. K. (2023). Plasma based fracking in unconventional shale–A review. Materials Today: Proceedings, 72, 2791-2795.

Kristensen, P. K., Niordson, C. F., & Martínez-Pañeda, E. (2021). An assessment of phase field fracture: crack initiation and growth. Philosophical Transactions of the Royal Society A, 379(2203), 20210021.

Miehe, C., Aldakheel, F., & Teichtmeister, S. (2017). Phase-field modeling of ductile fracture at finite strains: a robust variational-based numerical implementation of a gradient-extended theory by micromorphic regularization. International Journal for Numerical Methods in Engineering, 111(9), 816-863.

Liu, Y., Yoshioka, K., You, T., Li, H., & Zhang, F. (2024). A phase-field fracture model in thermo-poro-elastic media with micromechanical strain energy degradation. Computer Methods in Applied Mechanics and Engineering, 429, 117165.

Dai, Y., Hou, B., Lee, S., & Wick, T. (2024). A thermal–hydraulic–mechanical–chemical coupling model for acid fracture propagation based on a phase-field method. Rock Mechanics and Rock Engineering, 57(7), 4583-4605.

Mandal, T. K., Nguyen, V. P., & Wu, J. Y. (2019). Length scale and mesh bias sensitivity of phase-field models for brittle and cohesive fracture. Engineering Fracture Mechanics, 217, 106532.

Kumar, A., Bourdin, B., Francfort, G. A., & Lopez-Pamies, O. (2020). Revisiting nucleation in the phase-field approach to brittle fracture. Journal of the Mechanics and Physics of Solids, 142, 104027.